

Early stages of collective cell invasion: Biomechanics

R. González-Albaladejo*,^{1,2} M. Carretero**,^{2,3} and L. L. Bonilla***^{2,4}

¹*Sorbonne Université, Laboratoire de Physique Théorique et Hautes Energies,
CNRS, UMR 7589, 4 Place Jussieu,
75252 Paris Cedex 05, France*
*ORCID: 0000-0001-9560-5720

²*Gregorio Millán Institute for Fluid Dynamics,
Nanoscience and Industrial Mathematics,
Universidad Carlos III de Madrid, 28911 Leganés, Spain.*

³*Department of Mathematics, Universidad
Carlos III de Madrid, 28911 Leganés, Spain.*

**ORCID: 0000-0002-3517-4241

⁴*Department of Mathematics, Universidad
Carlos III de Madrid, 28911 Leganés, Spain.*

***Corresponding author. E-mail:

bonilla@ing.uc3m.es. ORCID: 000-0002-7687-8595

(Dated: February 13, 2026)

Abstract

The early stages of the collective invasion may occur by single mesenchymal cells or hybrid epithelial-mesenchymal cell groups that detach from cancerous tissue. Tumors may also emit invading protrusions of epithelial cells, which could be led (or not) by a basal cell. Here we devise a fractional step cellular Potts model comprising passive and active cells able to describe these different types of collective invasion before cells start proliferating. Durotaxis and active forces have different symmetry properties and are included in different half steps of the fractional step method. Compared with a single step method, fractional step produces more realistic cellular invasion scenarios with little extra computational effort. Biochemical mechanisms that determine how cells acquire their different phenotypes and cellular proliferation will be incorporated to the model in future publications.

1. INTRODUCTION

The invasion of a tissue by cancer cells is a crucial first step of metastasis [1, 2]. As cells move, they interact with the extracellular matrix (ECM), which plays an important role in cancer [3]. Consider a tumor comprising epithelial (E) cells that adhere to each other and form the cancerous tissue. There are several types of invasion into healthy tissue after cancer cells break the basal membrane surrounding the tumor: either by single cells or by groups of cells in a collective invasion [1, 3]. Collectively invading cells maintain cell-cell junctions, whereas individually invading cells fully detach from the rest of the tumor. Different types of invasion are as follows.

(i) E cells undergoing the epithelial-mesenchymal transition (EMT) [4] lose their apical-basal polarity and cell-cell adhesions and reorganize their cytoskeleton, eventually obtaining a mesenchymal (M) phenotype with front-back polarity that enables migration away from the tumor as single cells [2]. M cells are elongated, emit spindle-like (filopodia) or sheet-like (lamellipodia) protrusions and advance through adhesion-mediated tractions and ECM degradation [5]. The migration of M cells may pave a path through the ECM for E cells to follow [6]. In complex, heterogeneous ECM microenvironments, single cells may adopt a much faster amoeboid motion (about $10\mu\text{m}/\text{min}$ vs $0.3\mu\text{m}/\text{min}$): they become round, emit blebs or pseudopods, have short-term and weak attachments to the ECM, and can squeeze through ECM pores [5, 7, 8]. Computational models of amoeboid and mesenchymal migration are discussed in Ref. [5].

(ii) Collective invasion may occur in different ways. Hybrid epithelial/mesenchymal (E/M) cells are related to different stages of the EMT [4, 9], and migrate as small clusters. M and E/M cells at different stages of the EMT are found in a variety of tumors [4]. (iii) Cancer tissue forms protrusions comprising a number of E cells that are alike, in an instability similar to finger formation in wound healing [10], or (iv) the protrusions are led by basal cells.

Basal tumor cells have E phenotype and lead invasion without undergoing the EMT [11]. Biochemical cues, EMT and cellular Notch signaling may trigger the invasion and they are intimately connected to biomechanical cellular motion and interaction [2, 12–14].

Here we focus on the mechanical aspects of cellular motion and the early stages of invasion before cells proliferate. Our work provides a proof-of-concept biomechanics framework for invasion prior to cell proliferation, distinguishing it from biochemical EMT or signaling models. Starting from a cellular Potts model (CPM) [15, 16] that includes durotaxis [17], we add *novel active forces* that affect differently to epithelial, mesenchymal and hybrid cells: each cell type has a specific local stiffness threshold that characterizes its response to strain gradients. Thus, the EMT acts as a transition between different mechanical regimes: E cells are static and very adhesive, M cells are active, less adhesive and freer to move, whereas E/M hybrid cells combine both behaviors.

When implementing the mechanism involving interconnections among EMT, cancer stem cells and Notch-Jagged signaling [12], it is important to characterize the mechanics of different cell phenotypes. Bocci *et al* have modeled EMT, cancer stem cells and Notch signaling by sets of interconnected ordinary differential equations (ODEs) [12]. They have studied phenotypes associated to each of the three cycles and explained how treatments that inhibit some variable perform [12]. Distinguishing phenotypes and assigning them mechanical properties is of paramount importance when using a realistic computational tool such as the cellular Potts model (CPM) to characterize cellular motion [15–17]. For example, in early stage angiogenesis, the phenotype tip (leader), stalk (follower) or hybrid tip/stalk (leader/follower) cell depends on biochemical factors such as the content of VEGF and Delta protein in the cells and is determined by the ODEs of Notch signaling dynamics [18–20]. When using the CPM, the parameters measuring the phenotype sensitivity to mechanical and chemical cues as well as the ability to proliferate determine the behavior of the cells [21, 22]. It is crucial to appropriately select

the values of the different CPM parameters and to check the effects that changing them have on cell behavior [21]. Once this is known, appropriate parameter values and qualitative properties need to be assigned to cells according to their phenotype: sensitivity to chemotaxis and proliferation of tip, stalk and hybrid tip/stalk cells in the case of angiogenesis [21].

Collective cell invasion depends on the ECM structure. Its role in cell migration and morphogenesis is discussed in Ref. [23]. The interstitial ECM fills spaces between organs and it has fibrous proteins and proteoglycans that form 3D arrangements. The basement membrane ECM forms 2D sheet-like ECM that line organ boundaries [23]. The influence of a fibrous, cross-linked ECM (modeled by bead-springs) on cell motion modeled by a CPM is discussed in Ref. [24] whereas the emergence of different cell motility types from cell-matrix adhesion dynamics via a modified CPM is shown in Ref. [25]. For collective invasion of cancer cells, the relation between phenotypes within the EMT, Notch signaling and cancer stem cell cycles [12], and the mechanical part of the CPM has not been established. Recently, Hirway *et al* have incorporated EMT to the CPM of Ref. [17] by means of a set of ODEs for one type of cells and for the ECM [26] and for several cell types and for the ECM [28]. These ODEs include source terms dependent on junctional forces that are coupled to the equations of elasticity comprising the mechanical part of the model [26]. They determine the E, M and E/M phenotype of the cells, and each phenotype has different adhesion and proliferation properties. The resulting model has been used to describe tissue formation and a wound healing (scratch) assay in which the cells of a tissue close a space that has been opened in their midst [26]. In these simulations, the cells have to proliferate to complete the tissue or to close the opening. However, openings in experiments with epithelial tissue often close without cellular proliferation, either in wound healing assays [29] or in antagonistic migration assays [30].

Different experiments have shown different phases in migrating clusters of malignant cells that can be modeled using ideas from active matter [31].

Experiments, theory and numerical simulations have shown the existence of chiral currents in confined monolayers of highly active spindle-shaped human fibrosarcoma cells with sources of active forces at the interfaces [32]. Long range force transmission of mechanical origin fosters phenomena such as waves in antagonistic migration assays [33], stress fibres mechanics [34] and collective cell durotaxis [35]. Is it possible to include active forces in the CPM? Rens and Edelstein-Keshet have considered forces due to cell-cell adhesion and also active forces due to a two-state signaling protein inside cells: they modify the CPM energy to incorporate the solutions of reaction-diffusion equations for the concentrations of active/inactive protein states [36]. Their results include measured polarization of the cells and retraction or expansion of the cell boundary [36]. Including pseudopods in the CPM can be achieved by defining a persistence variable related to actin and adding appropriate terms to the CPM energy [37].

In this paper, we consider a circular aggregate comprising epithelial, mesenchymal and hybrid E/M cells and study their migration and invasion at times shorter than that of cellular division. Mesenchymal and hybrid E/M cells are subject to active forces that do not affect epithelial cells. Cells with different phenotypes have different adhesion parameters. Biochemical cues that include coupled EMT, cancer stem cell and Notch signaling dynamics will be incorporated in a subsequent paper. Our results show that mesenchymal and hybrid cells placed near the edges of the aggregate escape toward an attraction point as single cells and small aggregates, respectively. Hybrid cells are more effective in their migration. Our work is a proof of concept that a combination of cellular phenotypes and mechanical properties can model early individual and collective invasion of tissues with possible applications for tumors and cancer metastasis.

2. DYNAMICS OF CELLS ON A SUBSTRATE

For the biomechanics of invading cells, we will consider durotaxis, the propensity of cells to migrate up gradients of substrate rigidity [17, 38], and active forces that direct cells to migrate to other regions. Following van Oers *et al* [17], we assume that a strained ECM is stiffer along the strain orientation than perpendicular to it (strain stiffening), that the ECM is isotropic and linearly elastic, and that stiffness is an increasing, linear function of the local strain. To mimic the attraction of cells to a particular region, we shall assume that they are pushed towards the target by a repelling linear force.

2.1. Influence of Substrate on Cell Dynamics

To study the influence of substrate stiffness on cell behavior, we build upon the computational model introduced in Ref. [17] to which we add active migration forces.

2.1.1. Durotaxis

Durotaxis is modeled as in Ref. [17]. We solve the Navier equations for isotropic linear elasticity using the finite element method (FEM) as follows:

$$\mathbf{K}\mathbf{u} = \mathbf{f}, \quad \mathbf{f}_i = \mu \sum_j \mathbf{d}_{ij}. \quad (1)$$

Here \mathbf{K} is the stiffness matrix, \mathbf{u} the displacement vector at each node, and \mathbf{f} the force vector. The force \mathbf{f}_i at node i is the tension per unit length, μ , multiplied by the sum of distances $\mathbf{d}_{ij} = \mathbf{n}_j - \mathbf{n}_i$ between node i and its neighboring nodes j , where \mathbf{n}_i and \mathbf{n}_j are their respective positions. The force \mathbf{f}_i mimics the cell-shape dependent contractile forces exerted by the cells onto the ECM, it does not derive from a potential energy, and it gives experimentally plausible predictions for fibroblasts, endothelial cells, and keratocytes [39].

In the present CPM, the pixels \mathbf{x} of a square grid (or in a cube in 3D) have labels identifying them as part of a cell or the ECM. After a random pixel change $\mathbf{x} \rightarrow \mathbf{x}'$, the CPM uses the Metropolis algorithm to update an energy H defined on the pixels. The energy comprises a term enforcing cell volume, a contact term modeling cell-cell and cell-substrate adhesion and a term monitoring changes in strain. The probability of accepting a change ΔH in energy is 1 if $\Delta H < 0$ and $e^{-\Delta H/T}$ otherwise:

$$P(\Delta H) = \begin{cases} 1 & \text{if } \Delta H < 0 \\ e^{-\Delta H/T} & \text{if } \Delta H \geq 0 \end{cases}, \quad (2)$$

where the temperature parameter $T > 0$ controls the intrinsic cell motility. The change in energy (Hamiltonian) is

$$\Delta H = \Delta H_{volume} + \Delta H_{contact} + \Delta H_{strain}. \quad (3)$$

We have

$$H_{volume} = \sum_{\sigma \in cells} \lambda \left(\frac{a(\sigma) - A(\sigma)}{A(\sigma)} \right)^2, \quad (4)$$

$$H_{contact} = \sum_{\mathbf{x}, \mathbf{x}'} J(\sigma(\mathbf{x}), \sigma(\mathbf{x}')) (1 - \delta(\sigma(\mathbf{x}), \sigma(\mathbf{x}'))). \quad (5)$$

Here $a(\sigma)$ is the actual cell volume, $A(\sigma)$ the target (resting) volume, σ an integer representing the label of each cell and substrate, and λ is the strength of the volume constraint. $J(\sigma(\mathbf{x}), \sigma(\mathbf{x}')) \geq 0$ represents the adhesion strength between neighboring pixels \mathbf{x} and \mathbf{x}' , while δ is the Kronecker delta. Adhesion values for cell-cell interactions are larger than those for cell-substrate (e.g., $J_{cc} \approx 2J_{cs} = 2.5$).

The strain term in Eq. (3) captures cell responses to substrate stiffness gradients (durotaxis) [17]:

$$\Delta H_{strain} = -g(\mathbf{x}, \mathbf{x}') \lambda_{duro} [h(E(\epsilon_1))(\mathbf{v}_1 \cdot \mathbf{v}_m)^2 + h(E(\epsilon_2))(\mathbf{v}_2 \cdot \mathbf{v}_m)^2]. \quad (6)$$

Here $g(\mathbf{x}, \mathbf{x}')$ distinguishes extension (+1) and retraction (-1), λ_{duro} controls the strain contribution, and \mathbf{v}_m is a unit vector in the copy direction $\mathbf{x} - \mathbf{x}'$. The

eigenvalues ϵ_1 and ϵ_2 of the strain tensor are the principal strains, and the corresponding eigenvectors, \mathbf{v}_1 and \mathbf{v}_2 , provide the strain orientation. Writing now the strain tensor as a column vector, we have

$$\boldsymbol{\varepsilon} = \mathbf{B}\mathbf{u}_e, \quad (7)$$

where \mathbf{B} is the conventional strain-displacement matrix for a four-noded quadrilateral element, and \mathbf{u}_e are the node displacements related to the local strains.

In Eq. (6), the substrate stiffness measured by the ECM Young modulus, $E(\epsilon)$, depends linearly on the principal strains:

$$E(\epsilon) = E_0 \left[1 + \frac{\epsilon}{\epsilon_{st}} \delta(|\epsilon|, \epsilon) \right], \quad (8)$$

where ϵ_{st} adjusts stiffening. The sigmoidal function $h(E)$ regulates focal adhesion maturation based on threshold stiffness E_θ :

$$h(E) = \frac{1}{1 + e^{-\beta(E(\epsilon)-E_\theta)}}, \quad (9)$$

where β is the steepness of the sigmoid. In extension, $g = 1$ in Eq. (6), we use the value E_θ of the target pixel \mathbf{x}' , whereas we use the value E_θ of the source pixel \mathbf{x} in retraction, $g = -1$ in Eq. (6). This symmetry extension-retraction keeps the cohesion of the cells. Notice that the force vector in Eq. (1) changes the energy in Eq. (6) through its influence on the strain tensor that also modifies the substrate stiffness. The strain-driven energy change of Eq. (3) entering the Monte Carlo step is the effective force that moves the cells.

The parameter values we use agree with the methodology outlined in [17]. The two-dimensional computational domain (substrate) is defined by its size in pixels, with NV_x and NV_y representing the number of pixels along each side. Each pixel corresponds to a physical size of $dx = 2.5\mu\text{m}$ resulting in domain dimensions $Lx = NV_x \cdot dx$ and $Ly = NV_y \cdot dx$. In this section, we set $NV_x = NV_y = 300$, which gives a domain size of $750\mu\text{m} \times 750\mu\text{m}$. The parameter values listed in Table I are compatible with those in Ref. [17] and

capture the qualitative behavior of the system while ensuring numerical stability and consistency with experimental observations. We have included a reference adhesion parameter J_{ref} indicative of the adhesion moduli for the different cell phenotypes.

TABLE I. Parameter values.

Parameter	λ	λ_{duro}	T	ϵ_{st}	J_{ref}	μ	E_0	E_θ	β
Value	500	10	1	0.1	1.25	0.01	10	1-15	0.5
Unit	-	-	-	-	-	nN/ μm	kPa	kPa	kPa^{-1}

The interplay between strain and substrate stiffness creates a feedback loop that governs cell dynamics and collective behavior. When cells adhere to a deformable substrate, they exert traction forces that deform it. The deformation changes the substrate's stiffness, which in turn influences cell migration and adhesion dynamics. This feedback loop is governed by the strain-stiffening relationship in Eqs (7)-(8). The strain-induced changes in stiffness affect the Hamiltonian strain term through Eq (9). A more elaborated CPM model that explains durotaxis from cell-ECM forces and focal adhesion dynamics is presented in Ref. [40].

By means of Eqs (1)-(9), we have simulated the evolution of a circular agglomerate of red passive non-active cells with embedded blue active cells placed in random positions. The only differences among cells are their stiffness thresholds: $E_{\theta c} = 1 \text{ kPa}$ (passive cells) and $E_{\theta m} = 15 \text{ kPa}$ (active cells). Non-active cells maintain equilibrium under substrate rigidity, while active cells respond to strain gradients generated by passive cells. The result is that active cells move towards the borders of the agglomerate and may leave it, as shown in Fig 1. For further details, see Video S1.

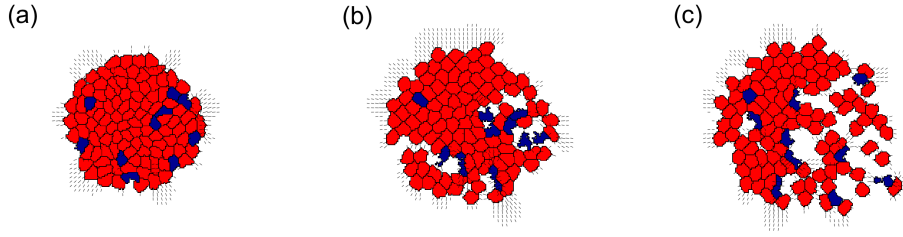


Fig 1. Simulated active and passive cells. Dynamics of red cells (passive, $E_{\theta c} = 1 \text{ kPa}$) and blue cells (active, embedded into a disk of passive cells, $E_{\theta m} = 15 \text{ kPa}$), with substrate strains (black arrows). Initial condition: circle-shaped distribution with 10 randomly placed blue cells. Panels show different iterations: (a) $t=50$, (b) $t=500$, (c) $t=1000$. See Video S1. Line segments indicate strain magnitude and orientation above a given threshold [17].

2.1.2. Incorporation of Migration Forces in the Model

To achieve directed migration of the active cells, we introduce a global long range active migration force \mathbf{f}_m . Long range force transmission of mechanical origin is responsible for phenomena such as waves in antagonistic migration assays [33], stress fibres mechanics [34], collective cell durotaxis [35], etc. The migration force must be incorporated into the finite element part of the model by modifying the Navier equation:

$$\mathbf{Ku} = \mathbf{f} + \mathbf{f}_m. \quad (10a)$$

Here, we propose an idealized simple long range migration force: \mathbf{f}_m is zero for passive cells, whereas it depends on the distance to a point of reference (push force) or to a point of attraction (pull force) for active cells. A push migration force on node i of the active cells is

$$\mathbf{f}_{mi} = \mu \mathbf{d}_{mi} = \mu (\mathbf{d}_m - \mathbf{d}_i), \quad (10b)$$

where \mathbf{d}_m is the position of a reference point opposite to the target location, and \mathbf{d}_i is the position of node i of the active cell. The force \mathbf{f}_m points towards d_m ,

away from the target point, and modifies the displacement \mathbf{u} , whose discrete gradient for an extension towards the target point is $0 - \mathbf{f}_{mi}$. In turn, this generates strains ε in Eq (7) whose magnitude increases with $|\mathbf{d}_m - \mathbf{d}_i|$. These strains enter the CPM through the durotaxis Eq. (6) and push the cell towards the target location (under cellular extension towards it). As an alternative to Eq. (10b), the pull migration force is

$$\mathbf{f}_{mi} = \mu \mathbf{d}_{ia} = \mu(\mathbf{d}_i - \mathbf{d}_a), \quad (10c)$$

where \mathbf{d}_a is the position of the target location (attraction point). The force \mathbf{f}_{mi} of Eq. (10c) also points away from the target location \mathbf{d}_a and pulls the cell towards the attraction point. The difference between push and pull forces is that the push force is stronger the further the distance to \mathbf{d}_m is (and therefore the shorter the distance to \mathbf{d}_a is), whereas the pull force is weaker the shorter the distance to \mathbf{d}_a is. The push force provides a more efficient attraction to the target point and therefore it is our force of choice.

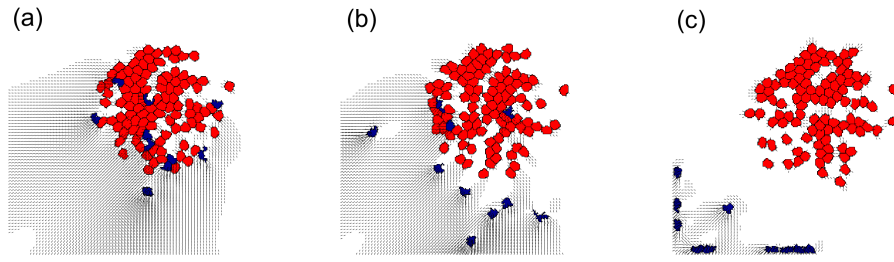


Fig 2. Simulated migration force. Migration of active blue cells ($E_{\theta m} = 15$ kPa) and passive red cells ($E_{\theta c} = 1$ kPa). Substrate strains are shown by black arrows. Blue cells are attracted to the lower left corner. The initial condition is the same as in Fig 1. Panels at iterations: (a) $t=1000$, (b) $t=1500$, (c) $t=3000$.

See Video S2.

The active force modifies the behavior of the active cells, directing them preferentially towards the point of attraction and away from the reference point: The strain gradient created by the migration force directs the movement of the

cells. Figure 2 shows how the active blue cells respond to the migration force by moving towards the attraction center whereas the passive red cells are insensitive to it. The black arrows represent the strains in the substrate, which are influenced by the migration force. These simulations illustrate the influence of substrate stiffness, active forces, and strain feedback on collective cell behavior. These mechanisms are crucial in tissue morphogenesis and the self-organization of cells into functional structures. Next, we specify different adhesion properties and threshold stiffnesses for cells of different phenotypes that are responsible for their diverse behavior.

2.2. Influence of Cell-Cell and Cell-Substrate Adhesion

To incorporate a hybrid cell type that exhibits both active behavior and a tendency to adhere to similar cells, we modify the cell-cell and cell-substrate adhesion parameters, $J(\sigma(\mathbf{x}), \sigma(\mathbf{x}'))$ in Eq (5). In this subsection, we analyze how these parameters influence the interactions between various cell types and the substrate, leveraging adhesion values from [15, 16] to identify distinct cellular phases. While phenotypes may result from cell biochemical processes (which we discuss in a forthcoming paper), we need to assign different mechanical properties to different cell types. In a similar vein, different mechanical properties are assigned to leader and follower (tip and stalk) cells resulting from Notch signaling dynamics in angiogenesis [21].

2.2.1. Pattern Types According to Adhesion Parameters

We consider two cell types (passive and active). Their adhesion dynamics depend on the stiffness thresholds ($E_{\theta c}$ for passive cells, $E_{\theta m}$ for active cells), the cell populations (N_m for active cells, N_c for passive cells, and N_{total} overall) and the cell-cell and cell-substrate adhesion parameters, $J(\sigma(\mathbf{x}), \sigma(\mathbf{x}'))$ in Eq (5). The latter adopt different values with respect to a reference adhesion J_{ref} , which we denote by

- $J_{cs} = j_{cs}J_{\text{ref}}$: passive cell-substrate adhesion,
- $J_{cc} = j_{cc}J_{\text{ref}}$: passive cell-passive cell adhesion,
- $J_{cm} = j_{cm}J_{\text{ref}}$: passive cell-active cell adhesion,
- $J_{mm} = j_{mm}J_{\text{ref}}$: active cell-active cell adhesion,
- $J_{ms} = j_{ms}J_{\text{ref}}$: active cell-substrate adhesion.

Lower (resp. higher) adhesion parameter values facilitate (resp. impede) adhesion. The relative values between adhesion parameters are critical: If $j_{cs} = j_{cm} > j_{cc}$ for example, passive cells prefer to adhere to each other preferably than adhering to the substrate or to active cells. Through a qualitative analysis, we have identified in the Supplementary Table S1 seven dynamic patterns based on variations in adhesion parameters, substrate stiffness, and cell populations:

1. *Clusters of passive and active cells sharing boundaries, each cell preferring their own type:* When $j_{cc} < j_{mm} \approx j_{cm} \approx j_{cs} \approx j_{ms}$, cells cluster with their own type, and secondarily with the opposite type, over sticking to the substrate. See Fig. 3(a).
2. *Separate clusters consisting of only passive or active cells with no inter-species adhesion:* Strong intra-species adhesion (j_{qq} , $q = c, m$) and weak inter-species adhesion, $j_{cm} \gg j_{qq}$, promote segregation. See Fig. 3(b).
3. *Separated passive and active cells, with unbound active cells:* Active cells exhibit weak interactions, while passive cells cluster tightly. Flexible substrates enhance active cell freedom. For structured separations, this pattern requires $j_{cm}, j_{mm} \gg j_{ms}$ and balanced populations, $N_m \approx N_c$. See Fig. 3(c).

4. *Disordered compact pattern with active cells forming the outer rim:* Cells of different species cluster together when inter-species adhesion dominates, $j_{cm} \ll j_{mm}$. See Fig. 3(d).
5. *Active cells push passive cells apart yielding a fragmented pattern:* active cells exert pressure, disrupting passive cell cohesion. Differences in stiffness thresholds, $E_{\theta c} \neq E_{\theta m}$, and low j_{ms}, j_{cm} drive this pattern. See Fig. 3(e).
6. *Single active cells escape from a cluster of passive cells, active cells are at the periphery and moving away:* Active cells surround passive cell groups when $j_{ms} \ll j_{mm}, j_{cm}$ and $N_m \ll N_c$. Passive cells act as the central reference group. See Fig. 3(f).
7. *Cluster metastasis: active cells form clusters around passive cells:* Active cells group together in a ‘metastasis’ configuration around passive cells when $j_{mm} \leq j_{ms} \ll j_{cm}$. See Fig. 3(g).

Figure 3 illustrates these patterns: It shows cellular configurations of types 1 to 7 as well as mixtures of different types in Figs. 3(h) and 3(i). To ensure reproducibility of our results, Supplementary Table S1 has 21 configurations and lists the conditions under which different patterns are found. For example, entry # 24 in the table combines configurations 2, 5, 7, 9, 21. It corresponds to an aggregate of 111 cells, of which 10 (a much smaller number) are active (configurations 2,5). The thresholds for stiffness (the Young modulus) in Eq. (9) are $E_{\theta c} = 1$ kPa (passive cells) and $E_{\theta m} = 15$ kPa (active cells) as in configuration 7. Thus, active cells move more easily than passive ones. The relative adhesion parameters are $j_{ms} = 1/4$, $j_{cs} = j_{cc} = j_{mm} = 1$, $j_{cm} = 10$, which correspond to configurations 9, 21. The adhesion parameter between active cells and substrate is smaller than that between passive cells and substrate and active-active and passive-passive cells, whereas the adhesion parameter between active and passive cells is much higher. With these values, active cells

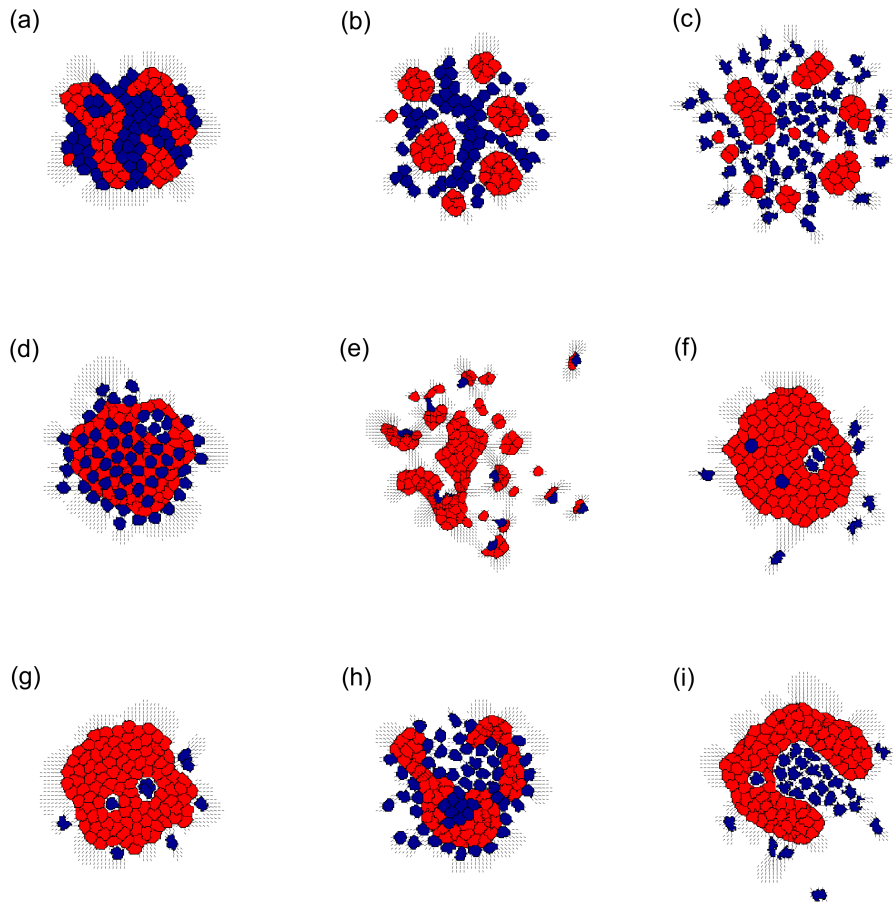


Fig 3. Changes in adhesion parameters. A total of $N_{total} = 111$ cells are randomly placed inside a circular enclosure, with N_m active cells (in blue) and passive adhesive cells (red). (a) $E_{\theta c} = E_{\theta m} = 1\text{kPa}$, $j_{cs} = 1$, $j_{cc} = 1/2$, $j_{cm} = 2$, $j_{ms} = 1$, $j_{mm} = 2$, $N_m = 56$. (b) same as (a) except $j_{cm} = 11$. (c) $E_{\theta c} = 1\text{kPa}$, $E_{\theta m} = 15\text{kPa}$, $j_{cs} = 1$, $j_{cc} = 1$, $j_{cm} = 4$, $j_{ms} = 1/4$, $j_{mm} = 6$, $N_m = 56$. (d) same as (a) except $j_{mm} = 10$. (e) $E_{\theta c} = 1\text{kPa}$, $E_{\theta m} = 15\text{kPa}$, $j_{cs} = 1$, $j_{cc} = 1/2$, $j_{cm} = 2$, $j_{ms} = 1$, $j_{mm} = 12$, $N_m = 10$. (f) $E_{\theta c} = 1\text{kPa}$, $E_{\theta m} = 15\text{kPa}$, $j_{cs} = 1$, $j_{cc} = 1$, $j_{cm} = 4$, $j_{ms} = 1/4$, $j_{mm} = 6$, $N_m = 10$. (g) same as (f) except $j_{cm} = 10$, $j_{ms} = 1/2$, $j_{mm} = 1/2$. (h) same as (a) except $j_{mm} = 3$. (i) same as (e) except $j_{cm} = 10$, $j_{ms} = 1/4$. At $t = 3000$, the corresponding pattern types are: (a) 1, (b) 2, (c) 3, (d) 4, (e) 5, (f) 6, (g) 7, (h) 1,2,3, and (i) 3,6.

tend to disassociate themselves from passive cells whereas adhesions between like cell types or with the substrate are much more favorable. The resulting pattern is number 6, corresponding to Fig. 3(f). Mixtures of patterns occur with intermediate parameter values, reflecting locally dependent choices by cells; see Supplementary Table S1.

2.2.2. Implementation of the Migration Force

Incorporating the active migration force to the CPM means solving Eqs. (2)-(10). Then the forces \mathbf{f} and \mathbf{f}_m contribute equally to the overall displacement vector \mathbf{u} according to Eq. (10a). This approach fails to generate sufficient active displacement when the Hamiltonian variation from strains generated by substrate forces (stiffness force plus migration force) is less important than that generated by contact interactions with other cells and the substrate (which depends on adhesion parameter values). In other words, migration becomes negligible for some configurations of adhesion parameters when the Hamiltonian variation due to stiffness is greater than that of the migration force.

To overcome this difficulty, we propose a fractional time step method. In this method, displacements due to stiffness-induced forces \mathbf{f} are computed at time $t = n$ ($n = 0, 1, 2, \dots$) and Eqs. (1)-(9) are solved. After this, we find a ‘migration’ displacement \mathbf{u}_m and the corresponding ‘migration’ strain by solving the Navier equation

$$\mathbf{K}\mathbf{u}_m = \mathbf{f}_m, \quad (11a)$$

at the intermediate time step $t = n + 1/2$. The migration displacement produces a strain

$$\varepsilon_m = \mathbf{B}\mathbf{u}_{em}, \quad (11b)$$

from which the Hamiltonian variation is

$$\Delta H_{\text{ mig}} = -g(\mathbf{x}, \mathbf{x}') \lambda_{\text{ mig}} [h(E(\epsilon_{m1}))(\mathbf{v}_1 \cdot \mathbf{v}_m)^2 + h(E(\epsilon_{m2}))(\mathbf{v}_2 \cdot \mathbf{v}_m)^2] \quad (11c)$$

We give equal weight to migration and stiffness-induced variations of energy, $\lambda_{mig} = \lambda_{strain}$. In Eq. (11c), the threshold energy E_θ is always that of the target pixel, both in extension and in retraction. This breaks the symmetry extension-retraction existing in the energy variation of Eq. (6) and facilitates motion of the cells in a preferred direction. The resulting new configuration is accepted according to the probability given by Eq. (2) with energy $\Delta H = \Delta H_{volume} + \Delta H_{contact} + \Delta H_{mig}$ instead of Eq. (3).

The two approaches can be summarized as follows:

- *Single time step*: Combines stiffness and migration forces in a single equation ($\mathbf{Ku} = \mathbf{f} + \mathbf{f}_m$) at the same time step. While simple to implement, this approach may fail to generate effective migration displacement under certain conditions.
- *Fractional time step*: Separates the stiffness ($\mathbf{Ku} = \mathbf{f}$) and migration ($\mathbf{Ku}_m = \mathbf{f}_m$) force computations into distinct time steps that have distinct strain tensors hence and energy changes. This method allows iterative updates to the Hamiltonian for stiffness forces at $t = n$ and migration forces at $t = n + 1/2$.

The flowcharts of the two approaches are presented in Appendix A.

As shown in Fig 4, the fractional time step method ensures that active cells reach the attraction point away from the reference point even under challenging adhesion configurations, outperforming the single time step approach. Consider the same configuration as in Fig. 3(f). In the absence of the migration force, active cells escape from the aggregate without a preferred direction; see Fig. 4(b). What happens when we add reference/attraction points and a migration force as in Figs. 4(c) and 4(d)? Cluster migration is easier to achieve as neighboring pixels with different stiffness thresholds generate a gradient directing movement toward the attraction point. However, migration sometimes fails when traction and migration forces are combined in a single time step as in Fig. 4(c) but the fractional step approach succeeds as shown by Fig.4(d).

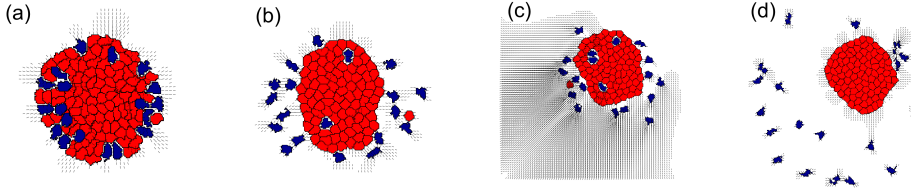


Fig 4. Comparison of migration force implementations. A total of $N_{total} = 111$ cells are randomly placed inside a circular enclosure, with $N_m = 19$ M cells (blue) and passive E cells (red). Parameter configuration as in Fig. 3(f): $E_{\theta c} = 1$ kPa, $E_{\theta m} = 15$ kPa, $j_{cs} = 1$, $j_{cc} = 1$, $j_{cm} = 4$, $j_{ms} = 1/4$, and $j_{mm} = 6$. (a) Initial configuration. At $t = 3000$: (b) No migration force, (c) migration forces with the single time step approach, and (d) migration forces with the fractional time step approach. The attraction point is located in the bottom-left corner.

Figure 5 shows further details on forces and strains as generated by the single step and fractional step methods on a 15-cell cluster out of which the three M cells have left. Panels (a), (f)-(j) have been produced by the fractional step method and the others by the single step method. Let us compare the strains in the ECM around the rightmost M cell (further from the reference point on the lower left corner and therefore closer to the target point on the upper right corner) as calculated by the single step method in Fig. 5(e) and the same strains calculated by the fractional step method in Fig. 5(j). The strains near the target point are greater when calculated by the fractional step method. Clearly, M cell invasion is much more facilitated by the fractional step method than by combining stiffness and migration forces as in the single step method.

Figure 6 presents two simulations of migration of M cells from a cellular aggregate formed by E and M cells with other adhesion parameters that make it harder for E and M cells to separate. The single time step approach succeeds for M cells to reach the attraction point if $j_{mm} = 1/2$ (low M-M cell adhesion, cf Fig. 6(c)), but fails if $j_{mm} = 1$ (larger M-M cell adhesion, cf Fig. 6(f)), whereas the fractional time step approach always enables migration; see Fig. 6(b) and

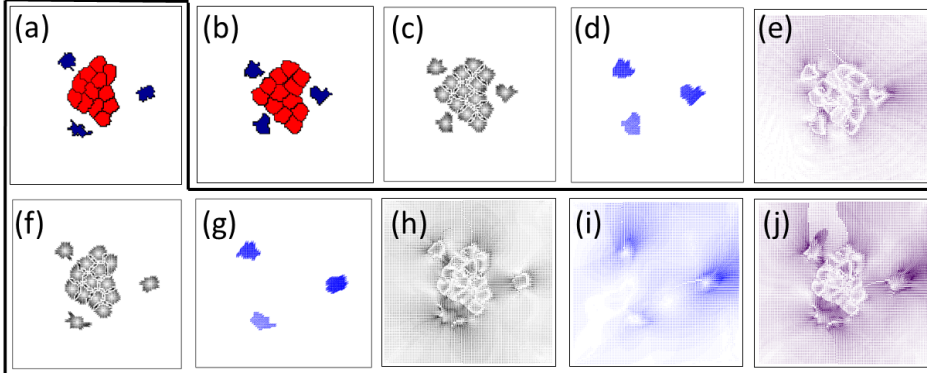


Fig 5. Forces and strains produced by the single and fractional step

methods. A cluster formed by 12 passive E cells (red) with 3 M cells (blue) on its boundary has evolved 500 Monte Carlo steps either by the fractional step method, Panels (a) and (f)-(j), or by the single step method, Panels (b)-(e). For Panel (b) (single step), (c) stiffness force f , (d) migration force f_m , (e) strain on ECM associated to force $f + f_m$. For Panel (a) (fractional step), (f) stiffness force f , (g) migration push force f_m , (h) strain on ECM associated to stiffness force f , (i) same for the migration force f_m , (j) sum of strains associated to stiffness and migration forces. Parameter values are as in Fig. 3(f) and the target point (not shown) is on the upper right corner. Panels (c)-(j) are density plots of the corresponding moduli, which are larger the darker the region is. The initial configuration is similar to that of Fig. 4(a) but with $N_{total} = 15$ cells.

6(e).

In qualitative terms, separating the steps of stiffness traction forces and migration forces is crucial. Stiffness forces as in Eq. (1) have extension-retraction symmetry by choosing the threshold energy E_θ corresponding to the target pixel for extension and to the source pixel for retraction. This ensures cohesive extension and retraction of the cells. Contrastingly, the migration forces of Eqs. (10) select the threshold energy of the target pixel both in extension and in retraction, which induces directional movement. Thus, the fractional time step approach provides a robust framework for modeling active migration and stiffness-driven mechanics for different

adhesion values. This method with the push forces of Eq. (10b) will be adopted in subsequent simulations.

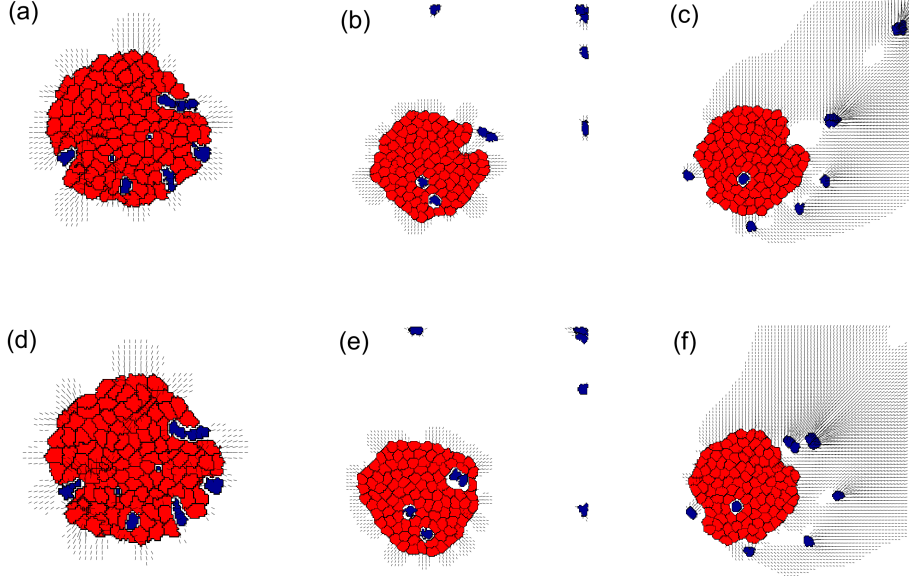


Fig 6. Migration forces and aggregate dynamics. The system consists of $N_{total} = 111$ cells, including $N_m = 10$ active cells, initially forming a circular aggregate. Parameter values are $E_{\theta c} = 1$ kPa, $E_{\theta m} = 15$ kPa, $j_{cs} = 1$, $j_{cc} = 1$, $j_{cm} = 10$, and $j_{ms} = 1$. First row, $j_{mm} = 1/2$: (a) Initial configuration at $t = 15$, (b) configuration at $t = 3000$ with the fractional time step approach differentiating between mechanical (stiffening) and active (migration) forces, and (c) configuration at $t = 3000$ with the single time step approach. Second row, $j_{mm} = 1$: (d) Initial configuration at $t = 15$, (e) configuration at $t = 3000$ with the fractional time step approach, and (f) configuration at $t = 3000$ with the single time step approach. The point of attraction is located in the upper-right corner of the enclosure. Cells in red have passive E phenotype, while cells in blue have active M phenotype. The full dynamics corresponding to panel (b) is in the Video S3.

a. *Computational Time Analysis.* Besides the qualitative differences in outcome explained above, the computational cost of the single step and

fractional step methods varies significantly. We shall compare the results of the fractional step approach in Figs. 4(d), 6(b) and 6(e) with those of the single step approach in Figs. 4(c), 6(c) and 6(f). Times were measured using a HP Laptop 15s-fq5xxx with processor 12th Gen Intel® Core™ i7-1255U (12 cores at 1.7 GHz), 16 GB RAM and 64 bit Windows 11 Home OS.

- Fig. 4(d) (fractional time step method) requires approximately 2.5 hours, compared to 45 minutes for Fig. 4(c) (single time step method).
- Fig. 6(f) (single time step) is completed in 1 hour, while Fig. 6(e) (fractional time step) takes 2 hours and 15 minutes.
- For Fig. 6(c) (single time step), the runtime is 1 hour and 45 minutes, compared to 2 hours and 15 minutes for Fig. 6(b) (fractional time step).

When migration fails under the single time step approach, Fig. 6(f), the fractional time step method requires more than double the computational time (over 100% longer, Fig. 6(e)). However, in cases where migration from the aggregate succeeds under single time step, as in Fig. 6(c), the additional computational cost for the fractional time step method of Fig. 6(b) is modest, approximately 30 minutes, representing a 30% increase ($t_f = 1.3t_s$, where t_f and t_s denote runtimes for the fractional and single time step methods, respectively). With respect to the single time step method, the computational cost of the fractional time step method does not scale linearly with its increased complexity. Precisely, the computational calculation is 2 times longer but the computational time is only 1.3 times larger. Thus, the computational cost is larger for the fractional step method and there are instances that fractional step captures the escape of individual cells while the single step method does not. In conclusion, while the fractional time step method introduces a slight additional computational cost, its robustness in enabling migration under varied adhesion parameters justifies its application in these scenarios.

3. RESULTS

In this section, we illustrate invasion by single cells from a circular aggregate (tumor) and collective invasion.

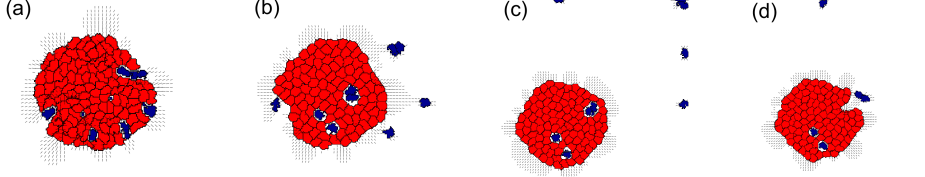


Fig 7. Computing the Migration Force with Clusters. A total of $N_{total} = 111$ cells are randomly placed inside a circular enclosure, with $N_m = 10$ active cells (blue) and passive adhesive cells (red). Parameter configuration: $E_{\theta c} = 1$ kPa, $E_{\theta m} = 15$ kPa, $j_{cs} = 1$, $j_{cc} = 1$, $j_{cm} = 10$, $j_{ms} = 1$, and $j_{mm} = 1/2$. Snapshots at: (a) $t = 15$, (b) $t = 300$, (c) $t = 2700$, and (d) $t = 3000$ with parallel migration force. The attraction point is located in the upper-right corner. See Supplementary Video S3.

Fig. 7 shows a circular aggregate of 111 cells, ten of which have M phenotype and are randomly placed, and the rest are E cells. We observe intrinsic patterns in Figs. 7(a) and 7(b), such as the elongation of individually migrating cells at the aggregate outer rim, surrounded by round E cells. The M cells escape and migrate effectively toward the attracting point at the upper right corner. Figs. 7(b)-(d) show other patterns: clusters of two M cells that move forward, break bonds with E cells and deform the outer rim of the aggregate; see Supplementary Video S3. Isolated M cells surrounded by E cells are trapped and cannot escape.

Hybrid E/M cells form clusters, migrate collectively. These cells are more adhesive than M cells but retain active traits, making them effective in metastasis. To model them, we assign them the same energy threshold as M cells, $E_{\theta m} = 15$ kPa, whereas E cells have $E_{\theta c} = 1$ kPa. In addition, we give hybrid cells specific adhesion parameters: j_{hs} , j_{hc} , j_{hm} , j_{hh} (hybrid-substrate,

hybrid-passive, hybrid-active, and hybrid-hybrid adhesion, respectively).

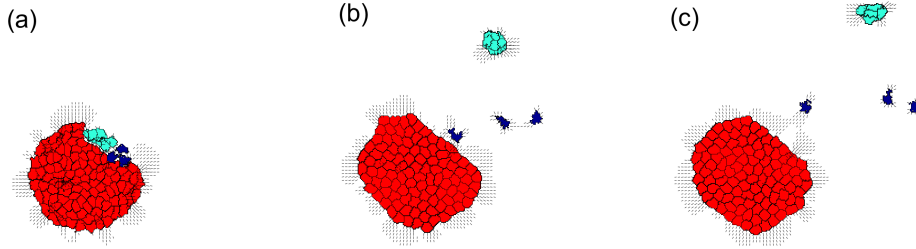


Fig 8. Simulation of adhesive, active, and hybrid cells. A total of $N_{total} = 111$ cells are randomly placed inside a circular enclosure, with $N_m = 3$ active cells (blue), $N_h = 4$ hybrid cells (light blue), and passive adhesive cells (red). Parameter configuration: $E_{\theta c} = 1$ kPa, $E_{\theta m} = 15$ kPa, $j_{cs} = 1$, $j_{cc} = 1$, $j_{cm} = 4$, $j_{ms} = 1/4$, $j_{mm} = 6$, $j_{hs} = 2$, $j_{hc} = 10$, $j_{hm} = 10$, and $j_{hh} = 1/2$. Snapshots at: (a) $t = 20$. (b) $t = 1500$. (c) $t = 3000$. active and hybrid cells are initially positioned near the attraction point in the upper-right corner. See Supplementary Video S4.

Fig 8 illustrates three cell types: E (red), M (blue), and E/M hybrid (light blue). M and hybrid cells are placed near the top corner, simulating local influences on phenotype. passive E cells have adhesion parameters that favor attachment to their own type, $j_{cs} = 1$, $j_{cc} = 1$, M cells have adhesion parameters that encourage them to remain isolated and interact primarily with the substrate, $j_{ms} = 1/4$, $j_{cm} = 4$, $j_{mm} = 6$, $j_{hm} = 10$, whereas hybrid cells exhibit a preference for clustering with their own kind but retain active behavior: $j_{hh} = 1/2$, $j_{hs} = 2$, $j_{hc} = 10$. Fig. 8 shows that N_h hybrid cells form clusters and consistently advance further than N_m M cells within the same time frame, which is consistent with known observations [1, 2]. See Supplementary Video S4 for the complete process.

A circular aggregate of epithelial cells can exhibit a fingering instability as in wound healing assays [10, 29]. This has already been captured by the CPM without migrating cells (see Figure 6 of Ref. [17]); see also Fig. 9. In the latter

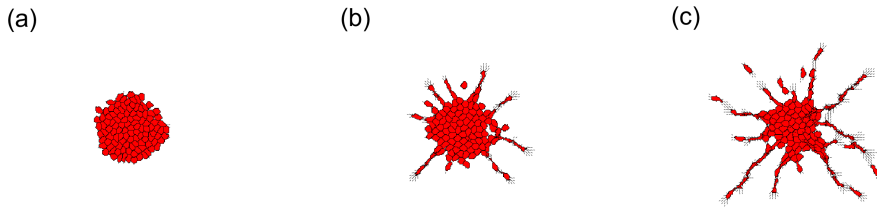


Fig 9. Invasion of tissue from fingering instability of a circular aggregate of epithelial cells. Parameter configuration: $N_{total} = 111$ cells, $E_{\theta c} = 10$ kPa, $j_{cs} = 1$, $j_{cc} = 2$. Snapshots at: (a) $t = 30$. (b) $t = 500$. (c) $t = 1000$. Note that individual cells and small cell clusters detach from the fingers. See Supplementary Video S5.

figure, the fingers of E cells resulting from the instability of the circular collectively invade the surrounding tissue. It is possible to model collective invasion of E cells led by a basal cell which is active and sense the attraction point whereas all other E cells are not active. See Fig. 10. Another possibility is to modify the adhesion parameter of a single E/M hybrid cell, which is justified as it is known that the EMT transition may exhibit different stages of completion [4, 9, 41].

4. DISCUSSION

We have proposed a biomechanical model of early invasion of cells that come from aggregates. Its basis is the cellular Potts model that incorporates durotaxis [17] modified to include active forces that affect differently mesenchymal (M), epithelial (E) and hybrid E/M cells. As we are interested in early stages, we have not included cellular proliferation. We have not included biochemical drivers such as chemotaxis, cellular Notch signaling, cancer stem cells or the EMT [12], which are left for a subsequent publication. Once the EMT model and the most relevant biochemical descriptions are determined for the particular cancer to

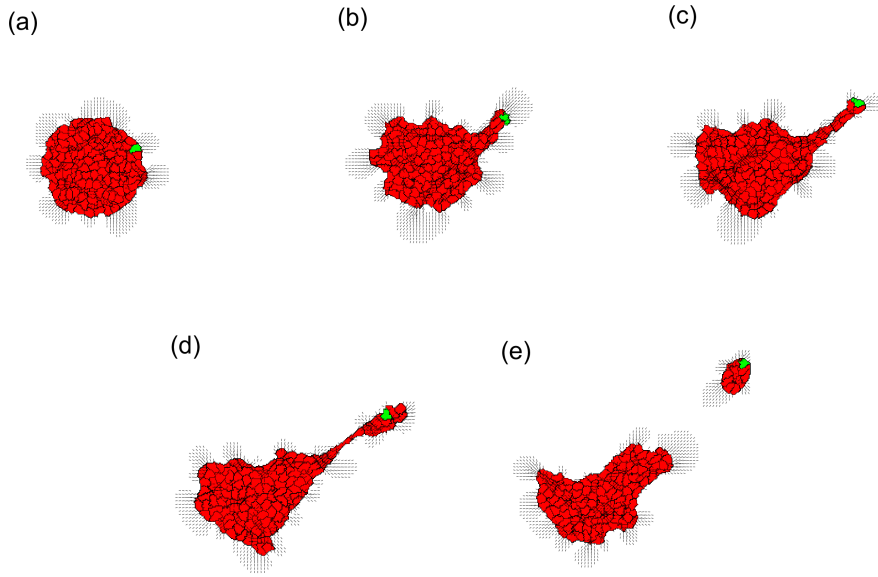


Fig 10. Invasion of tissue from finger formation led by a basal cell.

Parameter configuration: $N_{total} = 111$ cells, $E_{\theta c} = 10$ kPa, $j_{cs} = 1$, $j_{cc} = 1/2$.

Snapshots at: (a) $t = 30$. (b) $t = 500$. (c) $t = 1000$. (d) $t = 2000$. (e) $t = 3000$.

Note that a small cell cluster led by the green basal cell has detached from the finger. See Supplementary Video S6.

study [12–14, 27], these biochemical processes determine cell phenotypes that are assigned different mechanical characteristics as discussed in the present paper. This paper has implications for metastasis but our predictions are qualitative rather than quantitative until they are supplemented by future work.

As in previous works [17, 21], we have assumed that cells act as contractile units resulting in a first moment of area representation for their force distribution [39]. The resulting traction forces of the cells are realistic (but they *are not* the gradients of the CPM Hamiltonian) and the strains in the ECM are calculated via the finite-element method [17]. This approach produces cells moving by durotaxis. At a higher computational cost, traction forces consistent with the variations ΔH of the Hamiltonian in the CPM can be computed from the gradients of H using finite differences, interpolations and smoothing of pixels

in the CPM grid [36]. Here we have split each time step into two: For half a step, we have adopted the simpler durotaxis description of Ref. [17] and for the other half step we have used a simple model of active forces. Including more realistic active migration forces (e.g., nonlinear push and/or pull forces) is possible. For example, if certain cells move by chemotaxis in the gradient of a continuum field as in angiogenesis [21], the gradient of the corresponding term in the CPM Hamiltonian (calculated using finite differences, interpolation and smoothing [36]) produces active chemotactic forces. These forces could be incorporated via one half of a fractional time step while the traction forces of the cells comprise the other half step as in the present paper.

Our simulations highlight how substrate stiffness, substrate active forces and strain feedback loops drive collective cell behavior. These mechanisms are crucial in tissue morphogenesis, where cells migrate and self-organize into functional structures. The results also emphasize the role of heterogeneity in enabling emergent order in multicellular systems.

We have shown invasion by individual M cells coming from a circular aggregate that may model a cancerous tumor. In the absence of active forces, the M cells surround the tumor, as in Fig 4(b). This pattern is reminiscent of two-colored cancerous moles in some melanoma types where tissue of light color surrounds the darker nucleus; these tumors may eventually produce metastases [42]. Fig 4(d) is the visual pattern representing the activation of migration in such a tumor and, maybe, the initiation of metastasis. Our computational model also shows that collective invasion led by clusters of hybrid E/M cells is faster and more efficient than invasion led by M cells; see Fig. 8. In the future, we plan to incorporate the EMT, Notch signaling and cancer stem cells [12] to the present hybrid CPM.

SUPPORTING INFORMATION

Video S1. Active and passive single cells.

Video S2. Migration force in active cells.

Video S3. Migration patterns.

Video S4. Adhesive, active and hybrid cells.

Video S5. Collective invasion of E cells from a fingering instability.

Video S6. Collective invasion of E cells from a finger led by a basal cell.

ACKNOWLEDGMENTS

This work has been supported by the FEDER/Ministerio de Ciencia, Innovación y Universidades – Agencia Estatal de Investigación (MCIN/AEI/10.13039/501100011033) grants PID2020-112796RB-C22 and PID2024-155528OB-C22. Funding for APC: Universidad Carlos III de Madrid (Agreement CRUE-Madroño 2025).

- [1] P. Friedl J. Locker, E. Sahai, J. E. Segall, Classifying collective cancer cell invasion. *Nat. Cell Biol.* **14**, 777-783 (2012).
- [2] S. A. Vilchez Mercedes, F. Bocci, H. Levine, J. N. Onuchic, M. K. Jolly, P. K. Wong, Decoding leader cells in collective cancer invasion. *Nat. Rev. Cancer* **21**, 592-604 (2021).
- [3] J. J. F. Sleeboom, G. S. van Tienderen, K. Schenke-Layland, L. J. W. van der Laan, A. A. Khalil, M. M. A. Verstegen, The extracellular matrix as hallmark of cancer and metastasis: From biomechanics to therapeutic targets. *Sci. Transl. Med.* **16**, eadg3840 (2024).
- [4] I. Pastushenko, A. Brisebarre, A. Sifrim, M. Fioramonti, T. Revenco, S. Boumahdi, A. Van Keymeulen, D. Brown, V. Moers, S. Lemaire, S. De Clercq, E. Minguijón, C. Balsat, Y. Sokolow, C. Dubois, F. De Cock, S. Scozzaro, F. Sopena, A. Lanas, N. D'Haene, I. Salmon, J.-C. Marine, T. Voet, P.A. Sotiropoulou, C. Blanpain, Identification of the tumour transition states occurring during EMT. *Nature* **556**, 463-468 (2018).

[5] G. Shatkin, B. Yeoman, K. Birmingham, P. Katira, A. J. Engler, Computational models of migration modes improve our understanding of metastasis. *APL Bioeng.* **4**, 041505 (2020).

[6] C. Gaggioli, S. Hooper, C. Hidalgo-Carcedo, R. Grosse, J. F. Marshall, K. Harrington, E. Sahai, Fibroblast-led collective invasion of carcinoma cells with differing roles for RhoGTPases in leading and following cells. *Nat. Cell Biol.* **9**, 1392-1400 (2007).

[7] K. Pankova, D. Rosel, M. Novotny, J. Brabek, The molecular mechanisms of transition between mesenchymal and amoeboid invasiveness in tumor cells. *Cell Mol. Life Sci.* **67**, 63-71 (2010).

[8] K. Talkenberger, E. A. Cavalcanti-Adam, A. Voss-Bohme, A. Deutsch, Amoeboid-mesenchymal migration plasticity promotes invasion only in complex heterogeneous microenvironments. *Sci. Rep.* **7**, 9237 (2017)

[9] T. Brabletz, R. Kalluri, M. A. Nieto, R. A. Weinberg, EMT in cancer. *Nat. Rev. Cancer* **18**, 128-134 (2018).

[10] V. Hakim, P. Silberzan, Collective cell migration: A physics perspective. *Rep. Prog. Phys.* **80**, 076601 (2017).

[11] W. Choi, B. Czerniak, A. Ochoa, X. Su, A. Siefker-Radtke, C. Dinney, D. J. McConkey, Intrinsic basal and luminal subtypes of muscle-invasive bladder cancer. *Nat. Rev. Urol.* **11**, 400-410 (2014).

[12] F. Bocci, M. K. Jolly, J. T. George, H. Levine, J. N. Onuchic, A mechanism-based computational model to capture the interconnections among epithelial-mesenchymal transition, cancer stem cells and Notch-Jagged signaling. *Oncotarget* **9**(52), 29906-29920 (2018).

[13] S. A. Vilchez Mercedes, F. Bocci, M. Ahmed, I. Eder, N. Zhu, H. Levine, J. N. Onuchic, M. K. Jolly, P. K. Wong, Nrf2 regulates collective cancer migration by modulating the hybrid epithelial/mesenchymal phenotype. *Frontiers in Molecular Biosciences* **9**, 807324 (2022).

[14] N. Mukhtar, E. N. Cytrynbaum, L. Edelstein-Keshet, A multiscale computational model of YAP signaling in epithelial fingering behavior. *Biophys. J.* **121**, 1940-1948 (2022).

[15] F. Graner, J. A. Glazier, Simulation of biological cell sorting using a two-dimensional extended Potts model. *Phys Rev. Lett.* **69**(13), 2013-2016 (1992).

[16] J. A. Glazier, F. Graner, Simulation of the differential adhesion driven rearrangement of biological cells. *Physical Review E* **47**(3), 2128-2154 (1993).

[17] R. F. M. Van Oers, E. G. Rens, D. J. La Valley, C. A. Reinhart-King, R. M. H. Merks, Mechanical cell-matrix feedback explains pairwise and collective endothelial cell behavior in vitro. *PLoS Comput. Biol.* **10**(8), e1003774 (2014).

[18] M. Boareto, M.K. Jolly, E. Ben-Jacob, J.N. Onuchic, Jagged mediates differences in normal and tumor angiogenesis by affecting tip-stalk fate decision. *Proc. Natl. Acad. Sci. USA* **112**, E3836-E3844 (2015).

[19] M. K. Jolly, M. Boareto, M. Lu, J. N. Onuchic, C. Clementi, E. Ben-Jacob, Operating principles of Notch-Delta-Jagged module of cell-cell communication. *New J. Phys.* **17**, 055021 (2015).

[20] M. Boareto, M. K. Jolly, A. Goldman, M. Pietila, S. A. Mani, S. Sengupta, E. Ben-Jacob, H. Levine, J. N. Onuchic, Notch-jagged signalling can give rise to clusters of cells exhibiting a hybrid epithelial/mesenchymal phenotype. *Journal of the Royal Society Interface* **13**, 20151106 (2016).

[21] R. Vega, M. Carretero, R. D. M. Travasso, L. L. Bonilla, Notch signaling and taxis mechanisms regulate early stage angiogenesis: A mathematical and computational model. *PLoS Comput. Biol.* **16**(1), e1006919 (2020).

[22] R. Vega, M. Carretero, L. L. Bonilla, Anomalous angiogenesis in retina. *Biomedicines* **9**, 224 (2021).

[23] R. M. Crossley, S. Johnson, E. Tsingos, Z. Bell, M. Berardi, M. Botticelli, Q. J. S. Braat, J. Metzcar, M. Ruscone, Y. Yin, R. Shuttleworth, Modeling the extracellular matrix in cell migration and morphogenesis: A guide for the curious biologist. *Front. Cell Dev. Biol.* **12**, 1354132 (2024).

[24] E. Tsingos, B. H. Bakker, K. A. E. Keijzer, H. J. Hupkes, R. M H Merks, Hybrid cellular Potts and bead-spring modeling of cells in fibrous extracellular matrix. *Biophys. J.* **122**(13), 2609-2622 (2023).

[25] L. van Steijn, I. M. N. Wortel, C. Sire, L. Dupré, G. Theraulaz, R. M. H. Merks, Computational modelling of cell motility modes emerging from cell-matrix adhesion dynamics". *PLoS Comp. Biol.* **18**(2), e1009156 (2022).

[26] S. U. Hirway, C.A. Lemmon, S. H. Weinberg, Multicellular mechanochemical hybrid cellular Potts model of tissue formation during epithelial-mesenchymal transition. *Comput. Syst. Oncol.* **1**, e1031 (2021).

[27] S. U. Hirway, S. H. Weinberg, A review of computational modeling, machine learning and image analysis in cancer metastasis dynamics. *Comput. Syst. Oncol.* **3**, e1044 (2023).

[28] S. U. Hirway, K. G. Nairon, A. Skardal, S. H. Weinberg, A Multicellular Mechanochemical Model to Investigate Tumor Microenvironment Remodeling and Pre-Metapassive Niche Formation. *Cellular and Molecular Bioengineering* **17**, 573-596 (2024).

[29] L. Petitjean, M. Reffay, E. Grasland-Mongrain, M. Poujade, B. Ladoux, A. Buguin, P. Silberzan, Velocity fields in a collectively migrating epithelium. *Biophys. J.* **98**, 1790-1800 (2010).

[30] S. Moitrier, C. Blanch-Mercader, S. Garcia, K. Sliogeryte, T. Martin, J. Camonis, P. Marcq, P. Silberzan, I. Bonnet, Collective stresses drive competition between monolayers of normal and Ras-transformed cells. *Soft Matter* **15**, 537-545 (2019).

[31] K. Copenhagen, G. Malet-Engra, W. Yu, G. Scita, N. Gov, A. Gopinathan, Frustration-induced phases in migrating cell clusters. *Sci. Adv.* **4**, eaar8483 (2018).

[32] V. Yashunsky, D. J. G. Pearce, C. Blanch-Mercader, F. Ascione, P. Silberzan, L. Giomi, Chiral edge current in nematic cell monolayers. *Phys. Rev. X* **12**, 041017 (2022).

[33] P. Rodríguez-Franco, A. Brugués, A. Marín-Llauradó, V. Conte, G. Solanas, E. Batlle, J. J. Fredberg, P. Roca-Cusachs, R. Sunyer, X. Trepat, Long-lived force

patterns and deformation waves at repulsive epithelial boundaries. *Nature Mater.* **16**, 1029-1037 (2017).

[34] P. W. Oakes, E. Wagner, C. A. Brand, D. Probst, M. Linke, M. Glotzer, U. S. Schwarz, M. L. Gardel, Optogenetic control of RhoA reveals zyxin-mediated elasticity of stress fibres. *Nat. Comm.* **8**, 15817 (2017).

[35] R. Sunyer, V. Conte, J. Escribano, A. Elosegui-Artola, A. Labernadie, L. Valon, D. Navajas, J.M. García-Aznar, J.J. Muñoz, P. Roca-Cusachs, X. Trepas, Collective cell durotaxis emerges from long-range intercellular force transmission. *Science* **353**, 1157-1161 (2016).

[36] E. G. Rens, L. Edelstein-Keshet, From energy to cellular forces in the Cellular Potts Model: An algorithmic approach. *PLoS Comput. Biol.* **15**(12), e1007459 (2019).

[37] G. A. Burger, B. van de Water, S. E. Le Dévédec, J. B. Beltman, Density-dependent migration characteristics of cancer cells driven by pseudopod interaction. *Front. Cell Dev. Biol.* **10**, 854721 (2022).

[38] C.-M. Lo, H.-B. Wang, M. Dembo, Y.-L. Wang, Cell movement is guided by the rigidity of the substrate. *Biophys J.* **79**, 144-152 (2000).

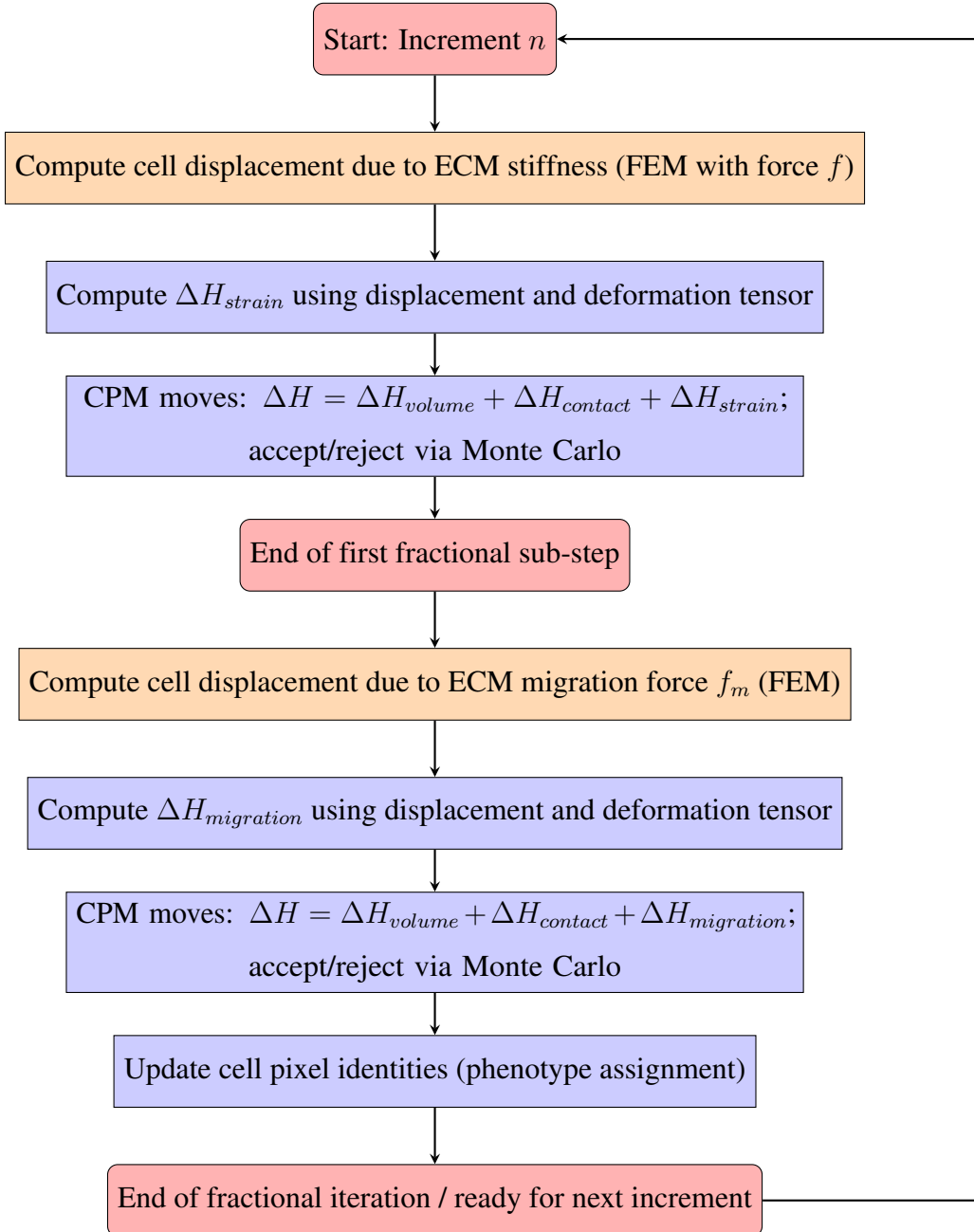
[39] C. A. Lemmon, L. H. Romer, A predictive model of cell traction forces based on cell geometry. *Biophys. J.* **99**, L78-L80 (2010).

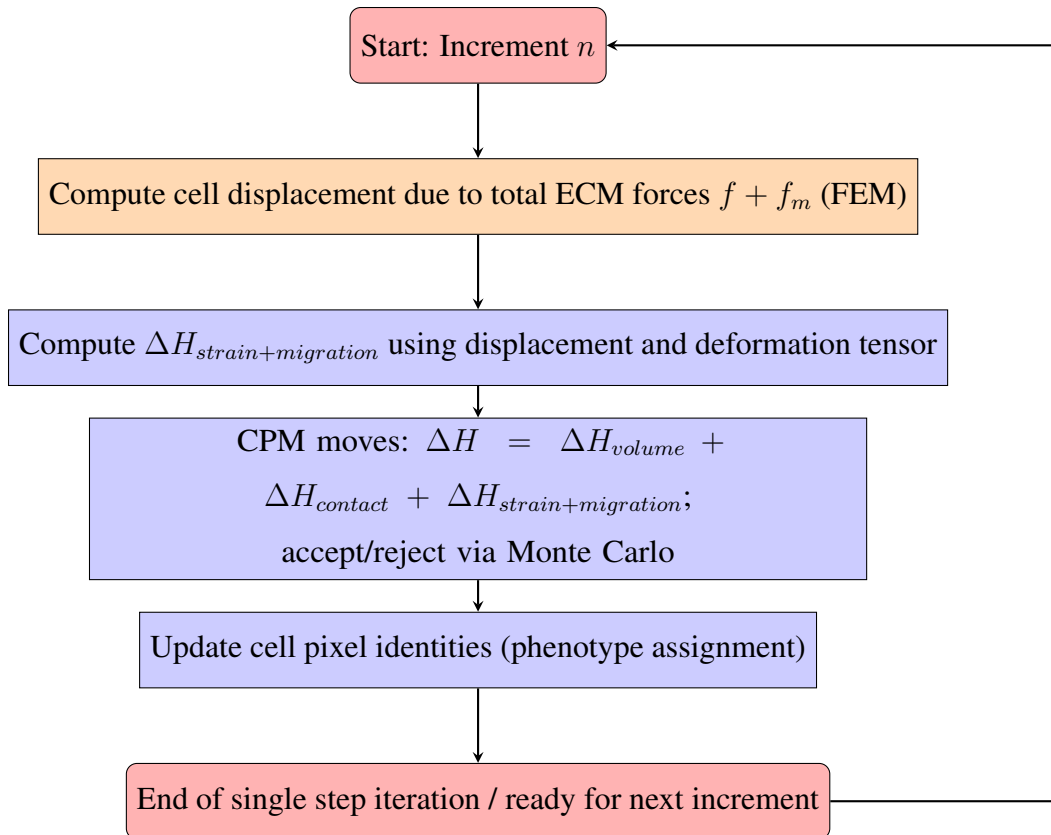
[40] E. G. Rens, R. M. H. Merks, Cell shape and durotaxis explained from cell-extracellular matrix forces and focal adhesion dynamics. *iScience* **23**(9), 101488 (2020).

[41] C. Kröger, A. Afeyan, J. Mraz, E. N. Eaton, F. Reinhardt, Y. L. Khodor, P. Thiru, B. Bierie, X. Ye, C. B. Burge, R. A. Weinberg, Acquisition of a hybrid E/M state is essential for tumorigenicity of basal breast cancer cells. *Proc. Natl. Acad. Sci. USA* **116**, 7353-7362 (2019).

[42] C. McCourt, O. Dolan, G. Gormley, Malignant melanoma: A pictorial review. *Ulster Med. J.* **83**(2), 103-110 (2014).

Appendix A: Flowcharts of the fractional step and single step methods





Supplementary Tables

- Configuration 1: Small N_{total} .
- Configuration 2: Large N_{total} .
- Configuration 3: Same ratio of active to passive cells $N_m \approx N_c \approx N_{total}/2$.
- Configuration 4: One-quarter active cells and three-quarters passive cells $N_m \approx N_c/3 \approx N_{total}/4$.
- Configuration 5: One tenth as many active cells as passive cells $N_m \approx N_c/10 \approx N_{total}/10$.
- Configuration 6: The stiffness threshold of the active ones with the substrate is the same as that of the passive ones $E_{\theta m} = E_{\theta c} = 1$.
- Configuration 7: The stiffness threshold of active species with different substrate than passive species $E_{\theta m} = 15 \neq E_{\theta c} = 1$.
- Configuration 8: The slightly preferred adhesion of passive cells is with themselves $j_{cc} \lesssim j_{cs}, j_{cm}$.
- Configuration 9: The slightly preferred adhesion of migrating cells is with the substrate $j_{ms} \lesssim j_{cm}, j_{mm}$.
- Configuration 10: The preferred adhesion of passive cells is with themselves $j_{cc} \ll j_{cs}, j_{cm}$.
- Configuration 11: the preferred adhesion par excellence of active cells is with the substrate $j_{ms} \ll j_{cm}, j_{mm}$.
- Configuration 12: Large penalisation in the adhesion of active-passive and active-active cells compared to other accessions $j_{cm} \approx j_{mm} \gg j$.
- Configuration 13: Slight penalisation in the adhesion of active-passive and active-active cells compared to the other adhesions. $j_{cm} \approx j_{mm} > j$.
- Configuration 14: Migrating cells prefer to adhere to passive cells rather than to themselves $j_{cm} < j_{mm}$.
- Configuration 15: active cells prefer to adhere to themselves rather than to passive cells $j_{mm} < j_{cm}$.
- Configuration 16: Preference in adhesion of passive cells to the substrate over other adhesions $j_{cs} < j$.
- Configuration 17: Penalisation of passive cell adhesion to the substrate compared to other adhesions $j < j_{cs}$.
- Configuration 18: passive and active ones have the same adhesion to the substrate $j_{cs} \approx j_{ms}$.
- Configuration 19: passive-active and passive-substrate adhesions are similar $j_{cm} \approx j_{cs}$.
- Configuration 20: active-active and active-substrate adhesion are similar and much lower than passive-active adhesion $j_{mm} \approx j_{ms} \ll j_{cm}$.
- Configuration 21: passive-passive and passive-substrate adhesion are similar and much lower than passive-active adhesion $j_{cc} \approx j_{cs} \ll j_{cm}$.

TABLE I. S1 Table of parameters and dynamic solutions.

#	Configurations	N_{total}	N_m	E_{dc} (kPa)	E_{dm} (kPa)	j_{cs}	j_{cc}	j_{cm}	j_{ms}	j_{mm}	Patterns
1	2, 5, 7, 20, 21	111	10	1	15	1	1	10	1/2	1/2	7
2	2, 5, 7, 20, 21	111	10	1	15	1	1	10	1/4	1/4	7
3	2, 5, 7, 20, 21	111	10	1	15	1	1	10	1/2	1/4	7
4	2, 5, 7, 20, 21	111	10	1	15	1	1	10	1	1	7
5	2, 5, 7, 20, 21	111	10	1	15	1	1	10	1	1/2	7
6	2, 5, 7, 21	111	10	1	15	1	1	10	2	1/2	7
7	2, 5, 7, 9, 20, 21	111	10	1	15	1	1	10	1/4	1/2	6-7
8	2, 5, 7, 8, 11, 12, 14	111	10	1	15	1	1/2	10	1/4	12	6
9	2, 5, 7, 10, 11, 12, 14	111	10	1	15	2	1/2	10	1/4	12	6
10	2, 5, 7, 10, 11, 12, 14	111	10	1	15	4	1/2	10	1/4	12	6
11	2, 5, 7, 10, 11, 12, 14	111	10	1	15	1	1/4	4	1/4	6	6
12	2, 5, 7, 8, 11, 12, 14	111	10	1	15	1	1/2	4	1/4	6	6
13	2, 5, 7, 8, 11, 13, 14	111	10	1	15	2	1	4	1/8	6	6
14	2, 5, 7, 8, 11, 13, 14	111	10	1	15	2	1	4	1/4	6	6
15	2, 5, 7, 11, 13, 14	111	10	1	15	1	1	4	1/4	6	6
16	2, 5, 6, 11, 13, 14	111	10	1	1	1	1	4	1/4	6	6
17	2, 5, 7, 11, 13, 14	111	10	1	15	1	1	4	1/2	6	6
18	2, 5, 7, 8, 11, 12, 14, 18	111	10	1	15	1	1/2	10	1	12	6
19	2, 5, 7, 8, 9, 13, 15	111	10	1	15	1	1/2	4	1	2	6
20	2, 5, 6, 8, 9, 13, 15	111	10	1	1	1	1/2	4	1	2	6
21	1, 3, 6, 8, 9, 14, 18	15	8	1	1	1	1/2	2	1	10	6
22	1, 3, 6, 8, 9, 13, 14, 18	15	8	1	1	1	1/2	2	1	3	6
23	1, 3, 6, 8, 9, 13, 18	15	8	1	1	1	1/2	2	1	2	6
24	2, 5, 7, 9, 21	111	10	1	15	1	1	10	1/4	1	6
25	2, 4, 7, 11, 13, 14	111	25	1	15	1	1	4	1/4	6	3-6
26	2, 4, 7, 8, 11, 12, 14	111	25	1	15	1	1/2	10	1/4	12	3-6
27	2, 4, 7, 10, 11, 13, 14	111	25	1	15	1	1/4	4	1/4	6	3-6
28	2, 5, 7, 10, 11, 14, 19	111	10	1	15	4	1/2	4	1/4	6	5
29	2, 5, 7, 8, 11, 14, 19	111	10	1	15	2	1	2	1/8	6	5
30	2, 5, 7, 8, 11, 13, 14	111	10	1	15	1	1/2	2	1/4	4	5
31	2, 5, 7, 8, 11, 14, 19	111	10	1	15	1	1/2	1	1/4	2	5
32	2, 5, 7, 8, 9, 13, 14, 18	111	10	1	15	1	1/2	3	1	5	5
33	2, 5, 7, 8, 9, 14, 18	111	10	1	15	1	1/2	2	1	12	5
34	2, 5, 6, 10, 14, 17, 18	111	10	1	1	1	1/8	11/16	1	14/16	4
25	2, 3, 6, 8, 9, 14, 18	111	56	1	1	1	1/2	2	1	10	4
36	2, 3, 6, 8, 9, 13, 14, 18	111	56	1	1	1	1/2	2	1	3	1-2-3
37	2, 5, 7, 11, 14	111	10	1	15	1	2	2	1/8	4	3
38	2, 3, 6, 8, 9, 13, 14, 18	111	56	1	1	1	1/2	3	1	5	3
39	2, 5, 7, 11, 12, 14, 16, 18	111	10	1	15	1	2	11	1	14	3
40	2, 5, 7, 9, 15, 16, 18	111	10	1	15	1	2	11	1	2	3
41	2, 3, 7, 11, 13, 14	111	56	1	15	1	1	4	1/4	6	3
42	2, 3, 7, 8, 11, 12, 14	111	56	1	15	1	1/2	10	1/4	12	3
43	2, 3, 7, 9, 15, 16, 18	111	56	1	15	1	2	11	1	2	2
44	2, 3, 7, 8, 9, 15, 18	111	56	1	15	1	1/2	11	1	2	2
45	2, 3, 6, 8, 9, 15, 18	111	56	1	1	1	1/2	11	1	2	2
46	2, 3, 7, 10, 15, 17, 18	111	56	1	15	1	1/4	1/2	1	1/3	1
47	2, 3, 6, 8, 9, 13, 18	111	56	1	1	1	1/2	2	1	2	1